

# Black hole images as probes of thermodynamic evolution

Lei You<sup>1,\*</sup> and Jinsong Yang<sup>1,†</sup>

<sup>1</sup>*School of Physics, Guizhou University, Guiyang 550025, China*

We investigate how black hole images (shadows and accretion–disk images) encode thermodynamic evolution information across different ensembles, using the Reissner–Nordström–AdS black hole as an illustrative example. Through analytic treatment and numerical verification, we demonstrate that these images encode not only phase transition information but also ensemble information, including additional temperature information in the isothermal ensemble. Phase transition information appears as a sudden increase in image size, which we prove occurs in both isobaric and isothermal ensembles. The ensemble and temperature information originates from a fundamental difference between isobaric and isothermal evolution: image size varies monotonically with the horizon radius along isobars, whereas it exhibits nonmonotonic behavior along isotherms. This contrast serves as a diagnostic tool to distinguish isobaric from isothermal evolution. In the isothermal ensemble, the nonmonotonic behavior introduces an extremal radius whose relative ordering with the small– and large–black hole radii at the phase transition admits three logical possibilities. Our analysis reveals that only two of these possibilities are physically realized, separated by a critical reduced temperature. Furthermore, image evolution in the two resulting temperature intervals exhibits qualitative differences, demonstrating that black hole images indeed encode temperature information. These results not only enrich the set of observational avenues for probing black hole thermodynamic properties, but also introduce a new paradigm. This paradigm studies phase transitions in conjunction with nonmonotonic evolution, providing a useful framework for exploring thermodynamic imprints in other black hole systems.

## I. INTRODUCTION

The advent of horizon–scale imaging, marked by the Event Horizon Telescope’s observation of the black hole in M87, has opened a new observational window onto black holes [1]. Motivated by this breakthrough, a large body of theoretical work has emerged, ranging from purely geometric analyses of black hole shadows and accretion–disk images to studies exploring how microscopic physics may imprint itself on observable optical appearances [2–11]. Among these developments, the connection between black hole thermodynamics and optical observables has proved particularly intriguing.

This connection originates largely from phase transitions in black hole thermodynamics. Following Hawking’s seminal discovery of black hole phase transitions, the interpretation of the cosmological constant as a dynamical pressure and of the black hole mass as enthalpy led to the framework of extended phase space in Anti-de Sitter (AdS) spacetimes [12–15]. Within this framework, charged AdS black holes exhibit Van der Waals–like small–/large–black hole phase transitions and critical phenomena, while higher–curvature theories and nonlinear electrodynamics give rise to reentrant phase transitions, triple points, and other exotic behaviors [16–25]. Building on these phase transition phenomena, researchers have progressively explored their associated optical imprints.

A representative example is the work of Wei *et al.*, who showed in the isobaric ensemble that replacing the horizon radius  $r_h$  with the photon–sphere radius  $r_{ps}$  yields a temperature function  $T(r_{ps})$  that still encodes phase transition behavior [26, 27]. This observation implies that a thermodynamic phase transition can induce a sudden change in optical appearance, providing a potential observational handle on black hole

phase transitions. This idea was later formalized by Zhang *et al.* in terms of the monotonicity of the function  $r_{ps}(r_h)$ , who proved that in spherically symmetric spacetimes  $r_{ps}(r_h)$  is monotonic, naturally leading to optical discontinuities at thermodynamic phase transitions [28, 29].

Recently, however, we showed that this monotonicity need not persist when multiple black hole parameters vary simultaneously. Using the Reissner–Nordström–AdS (RN–AdS) black hole as an example, we found that  $r_{ps}(r_h)$  is monotonic along isobaric evolution but becomes nonmonotonic along isothermal paths [30]. This phenomenon naturally prompts further reflection: Previous studies, by focusing primarily on phase transitions, effectively treated optical observables as static order parameters and could therefore identify only whether a phase transition occurs. Other thermodynamic information remained largely unexplored. From an evolutionary perspective, however, the emergence of nonmonotonic behavior in  $r_{ps}(r_h)$  suggests that the evolution of black hole images may encode ensemble information. Moreover, when phase transitions are considered together with such nonmonotonic behavior, black hole images may carry additional thermodynamic information beyond the occurrence of a transition itself. Exploring these possibilities is the central aim of this work.

We take the RN–AdS black hole as a concrete example and investigate how its shadow and accretion–disk images evolve along isobaric and isothermal thermodynamic ensembles. The paper is organized as follows. In Sec. II, we briefly review the basic framework of black hole shadow and accretion–disk imaging to set the stage for later analysis. In Sec. III, combining analytic arguments with numerical calculations, we study the evolution of these images in the two ensembles, relate their behaviors to black hole phase transitions, and explore how additional thermodynamic information can be extracted from black hole images. Finally, Sec. IV contains our discussion and conclusions. Throughout this paper we work in natural units with  $G = c = 1$ .

\* gs.lyou25@gzu.edu.cn

† Corresponding author; jsyang@gzu.edu.cn

## II. GEODESICS AND BLACK-HOLE IMAGING

In this section we briefly review the basic ingredients of black hole imaging and derive the formulas that will be employed in the next section.

The line element of the four-dimensional RN–AdS black hole reads

$$ds^2 = -f(r) dt^2 + f(r)^{-1} dr^2 + r^2(d\theta^2 + \sin^2\theta d\phi^2), \quad (2.1)$$

with

$$f(r) = 1 - \frac{2M}{r} + \frac{Q^2}{r^2} + \frac{r^2}{\ell^2}. \quad (2.2)$$

Here  $M$  and  $Q$  denote the black hole mass and electric charge, respectively, while  $\ell$  is the AdS curvature radius associated with the cosmological constant. In the extended phase-space formulation of black hole thermodynamics,  $\ell$  is related to the thermodynamic pressure  $P$  via

$$P = \frac{3}{8\pi\ell^2}, \quad \ell = \sqrt{\frac{3}{8\pi P}}. \quad (2.3)$$

In the limit  $\ell \rightarrow \infty$  (equivalently  $P \rightarrow 0$ ), the metric (2.2) reduces to the asymptotically flat RN spacetime.

The motion of a test particle in a static, spherically symmetric spacetime is described by the Lagrangian

$$2\mathcal{L} = g_{\mu\nu}\dot{x}^\mu\dot{x}^\nu = -\varepsilon, \quad \varepsilon = \begin{cases} 1, & \text{timelike particle,} \\ 0, & \text{photon,} \end{cases} \quad (2.4)$$

where the overdot denotes differentiation with respect to an affine parameter. Substituting the metric (2.2) into the above expression yields

$$2\mathcal{L} = -f(r)\dot{t}^2 + f(r)^{-1}\dot{r}^2 + r^2\dot{\theta}^2 + r^2\sin^2\theta\dot{\phi}^2 = -\varepsilon, \quad (2.5)$$

which does not depend explicitly on  $t$  or  $\phi$ , and hence one can define two conserved quantities,

$$E := -\frac{\partial\mathcal{L}}{\partial\dot{t}} = f(r)\dot{t}, \quad (2.6)$$

$$L := \frac{\partial\mathcal{L}}{\partial\dot{\phi}} = r^2\sin^2\theta\dot{\phi}, \quad (2.7)$$

corresponding to the energy and angular momentum of the particle, respectively. Solving the above relations for  $\dot{t}$  and  $\dot{\phi}$  and substituting them into Eq. (2.5), one obtains the radial equation of motion (fixing  $\theta = \pi/2$ ),

$$\dot{r}^2 = E^2 - f(r)\left(\varepsilon + \frac{L^2}{r^2}\right). \quad (2.8)$$

For photons ( $\varepsilon = 0$ ), the energy  $E$  can be absorbed by the reparametrization  $\lambda \rightarrow \lambda E$ , and the radial equation then simplifies to

$$\dot{r}^2 = 1 - b^2 U(r), \quad (2.9)$$

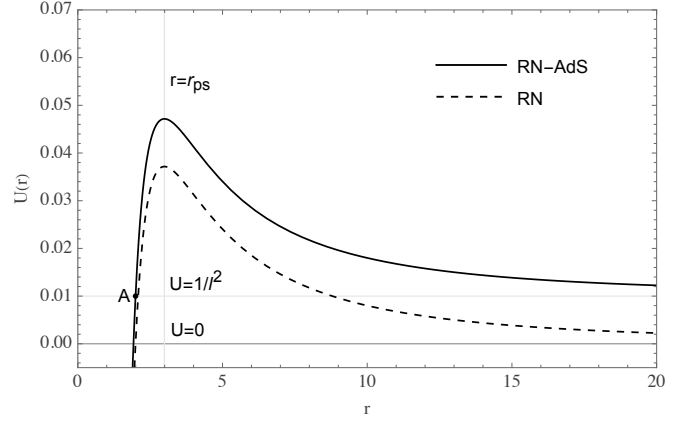


FIG. 1. Effective potential  $U(r)$  for the RN–AdS and asymptotically flat RN black holes.

where  $b := L/E$  is the impact parameter and  $U(r) := f(r)/r^2$  is the effective potential.

Figure 1 compares the effective potentials of RN–AdS and RN black holes, showing that the photon dynamics is qualitatively similar in the two spacetimes, except for a crucial difference at large radii: while the RN effective potential vanishes asymptotically, the RN–AdS potential approaches a positive constant,

$$\lim_{r \rightarrow \infty} U(r) = \lim_{r \rightarrow \infty} \left( \frac{1}{r^2} - \frac{2M}{r^3} + \frac{Q^2}{r^4} + \frac{1}{\ell^2} \right) = \frac{1}{\ell^2}. \quad (2.10)$$

As a consequence, the condition  $\dot{r}^2 \geq 0$  implies that photons with  $b \geq \ell$  can propagate only within a finite radial interval  $r \leq r_A$ , where  $r_A$  is defined by the intersection of  $U(r)$  with  $1/\ell^2$  (point A in Fig. 1). Therefore, for an observer located at  $r_0 > r_A$ , such photons can never reach the observer and do not contribute to the black hole image. In this work the observer is always placed outside the unstable photon sphere, i.e., at  $r_0 > r_{ps}$ , where  $r_{ps}$  is defined by  $dU/dr = 0$ . Since  $r_{ps}$  always lies outside  $r_A$ , the condition  $r_0 > r_A$  is automatically satisfied. Finally, only photons with  $b < \ell$  contribute to the image, and their trajectories on the equatorial plane obtained by eliminating the affine parameter between Eqs. (2.7) and (2.9) obey

$$\frac{dr}{d\phi} = \pm \frac{r^2}{b} \sqrt{1 - b^2 \frac{f(r)}{r^2}}, \quad (2.11)$$

where “+” (“−”) corresponds to outgoing (ingoing) motion. We denote its solution by  $r(\phi; b)$ , which allows us to construct the accretion-disk image in a ray-tracing scheme. Specifically, we launch photons from the observer with an emission angle  $\xi$ , defined as the angle between the photon direction and the local radial direction toward the black hole, which directly measures the apparent angular size of the image on the observer’s sky and is related to the photon impact parameter through [31]

$$\sin \xi = \frac{b \sqrt{f(r_0)}}{r_0}. \quad (2.12)$$

Among these rays, those intersecting the accretion disk satisfy

$$r(\phi_n; b_n(\xi_n)) = r_e, \quad (2.13)$$

where  $r_e$  denotes the orbital radius of the emitting disk particle. In this work we take

$$r_e \in [r_{\text{isco}}, +\infty), \quad (2.14)$$

with  $r_{\text{isco}}$  the radius of the innermost stable circular orbit (ISCO) of timelike particles ( $\varepsilon = 1$ ), determined by

$$\dot{r} = 0, \quad \frac{d\dot{r}}{dr} = 0, \quad \frac{d^2\dot{r}}{dr^2} = 0, \quad (2.15)$$

where  $\dot{r}$  is given by the radial equation (2.8) evaluated at  $\varepsilon = 1$ . The azimuthal angle  $\phi_n$  denotes the angle accumulated by a photon when it intersects the accretion disk. Since we consider only observers located above the north pole of the black hole,  $\phi_n$  takes the simple form

$$\phi_n = -\frac{\pi}{2} + n\pi, \quad n = 1, 2, \quad (2.16)$$

which correspond to the standard primary ( $n = 1$ ) and secondary ( $n = 2$ ) images in classical accretion-disk lensing theory. Then, solving Eq. (2.13) for  $b_n$  and substituting it into Eq. (2.12), the angular size of the accretion-disk image is obtained as

$$\xi_n = \arcsin\left(\frac{b_n \sqrt{f(r_0)}}{r_0}\right), \quad (2.17)$$

which in general admits no closed-form expression and is therefore evaluated numerically in the next section. By contrast, the angular size of the black hole shadow can be obtained analytically as

$$\xi_c = \arcsin\left(\frac{b_c \sqrt{f(r_0)}}{r_0}\right), \quad (2.18)$$

where

$$b_c = \frac{r_{\text{ps}}}{\sqrt{f(r_{\text{ps}})}} \quad (2.19)$$

is the critical impact parameter separating photons captured by the black hole from those escaping to large distances. In the next section, we exploit this analytic expression for the shadow to investigate how different thermodynamic ensembles imprint distinct signatures on black hole images.

### III. IMAGE EVOLUTION IN DIFFERENT ENSEMBLES

In this section we investigate how black hole images evolve in the isobaric and isothermal ensembles. Before proceeding, we briefly recall the distinct behavior of the photon-sphere radius  $r_{\text{ps}}$  in these two ensembles, which is governed by the monotonicity criterion [30]

$$\frac{dr_{\text{ps}}}{dr_h} = -\frac{1}{\Gamma_0} \frac{dM}{dr_h} \partial_M \Phi_0. \quad (3.1)$$

For RN-AdS black holes,  $\Gamma_0 < 0$  while  $\partial_M \Phi_0 > 0$ , so that along any thermodynamic evolution the monotonic behavior of  $r_{\text{ps}}(r_h)$  is determined solely by  $dM/dr_h$  (see Ref. [30] for a detailed analysis). Since  $dM/dr_h$  behaves differently in the isobaric and isothermal ensembles, the photon-sphere radius exhibits qualitatively distinct evolutions in the two cases.

In the isobaric case the pressure  $P$  is fixed and  $M(r_h)$  is determined from  $f(r_h; M) = 0$ , yielding

$$M(r_h) = \frac{3Q^2 + 3r_h^2 + 8\pi P r_h^4}{6r_h}. \quad (3.2)$$

Mathematically this function decreases for small  $r_h$  before rising at larger  $r_h$ . Physically, however, the first law of black hole thermodynamics,  $dM = T dS$ , imposes the constraint

$$\frac{dM}{dr_h} = 2\pi r_h T > 0, \quad (3.3)$$

where  $T$  denotes the Hawking temperature and  $S = \pi r_h^2$  is the Bekenstein-Hawking entropy. Consequently only the monotonic branch is admissible, and the curve must be cut at its minimum,

$$r_{h,\text{min}} = \frac{1}{4} \sqrt{-\frac{1}{\pi P} + \frac{\sqrt{1 + 32\pi P Q^2}}{\pi P}}, \quad (3.4)$$

beyond which  $M(r_h)$  increases monotonically.

In contrast, along an isothermal path both  $M$  and  $P$  vary and are constrained by the horizon condition  $f(r_h; M, P) = 0$  together with the isothermality condition  $T(r_h; M, P) = T_0$ , which yield

$$M(r_h) = \frac{2Q^2 + r_h^2 + 2\pi T_0 r_h^3}{3r_h}, \quad (3.5)$$

$$P(r_h) = \frac{Q^2 - r_h^2 + 4\pi T_0 r_h^3}{8\pi r_h^4}. \quad (3.6)$$

Mathematically,  $M(r_h)$  again decreases at small  $r_h$  before increasing at larger  $r_h$ . Physically, however, the first law now takes its extended form,  $dM = T dS + V dP$ , which implies

$$\frac{dM}{dr_h} = 2\pi r_h T + V \frac{dP}{dr_h}. \quad (3.7)$$

Compared with Eq. (3.3), the extended first law introduces an additional term  $V dP/dr_h$ , where the thermodynamic volume satisfies  $V > 0$  and  $dP/dr_h$  exhibits a characteristic van der Waals-type behavior, becoming strongly negative at small  $r_h$ . As a result,  $dM/dr_h$  can vanish or even turn negative, so  $M(r_h)$  no longer needs to be truncated and its nonmonotonic behavior is preserved.

These distinct behaviors of  $M(r_h)$  in the two ensembles lead directly to different monotonic properties of the photon-sphere radius  $r_{\text{ps}}(r_h)$ . Figure 2 displays the corresponding numerical results, which are fully consistent with the above analysis. Given the central role of the photon sphere in black hole imaging, it is then natural to expect that both the shadow and

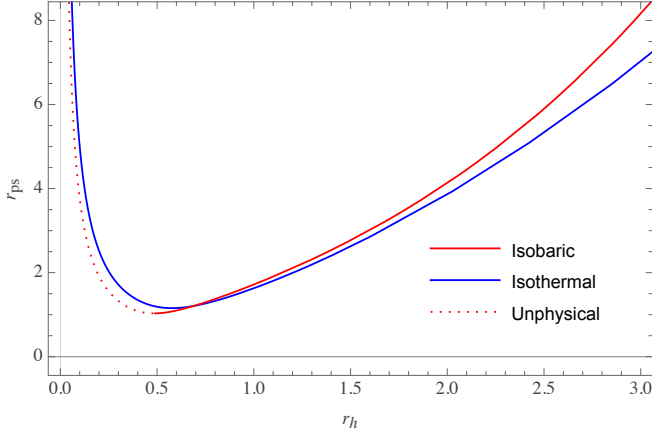


FIG. 2. Evolution of the photon-sphere radius  $r_{\text{ps}}$  as a function of the horizon radius  $r_h$  in the isobaric and isothermal ensembles.

accretion-disk images inherit these monotonic or nonmonotonic features. If so, the evolution of black hole images may provide an observational handle for distinguishing different thermodynamic processes.

We now begin a systematic analysis of how black hole images evolve under different thermodynamic ensembles, combining analytic arguments with numerical calculations. The analytic part focuses on the black hole shadow, since only the critical angle  $\xi_c$  admits a simple closed-form expression, whereas accretion-disk images generally do not.

The shadow angle given in Eq. (2.18) can be equivalently written as

$$\xi_c = \arcsin \left[ \frac{\sqrt{U(r_0)}}{\sqrt{U(r_{\text{ps}})}} \right] \equiv \arcsin(h). \quad (3.8)$$

where  $h$  (and hence  $\xi_c$ ) depends on  $r_h$  through  $M(r_h)$ ,  $\ell(r_h)$  (or equivalently  $P(r_h)$ ), and  $r_{\text{ps}}(r_h)$ . Since the arcsin function is monotonic on its domain,  $\xi_c(r_h)$  and  $h(r_h)$  share the same monotonic behavior, and it therefore suffices to analyze the latter. Differentiating  $h(r_h)$  with respect to  $r_h$  yields

$$\frac{dh}{dr_h} = \frac{g}{2U(r_{\text{ps}})}, \quad (3.9)$$

with

$$g = h^{-1} \frac{dU(r_0)}{dr_h} - h \frac{dU(r_{\text{ps}})}{dr_h}. \quad (3.10)$$

Since  $U(r_{\text{ps}}) > 0$ , the monotonic behavior of  $h(r_h)$  (and hence of  $\xi_c(r_h)$ ) is entirely determined by the sign of  $g$ . For convenience, we instead examine

$$hg = \frac{dU(r_0)}{dr_h} - h^2 \frac{dU(r_{\text{ps}})}{dr_h}, \quad (3.11)$$

whose sign is identical to that of  $g$ , because  $0 \leq h \leq 1$ . Using the chain rule (with  $P$  replacing  $\ell$ ), one obtains

$$\frac{dU(r_0)}{dr_h} = \frac{\partial U(r_0)}{\partial M} \frac{dM}{dr_h} + \frac{\partial U(r_0)}{\partial P} \frac{dP}{dr_h}, \quad (3.12)$$

and

$$\frac{dU(r_{\text{ps}})}{dr_h} = \frac{\partial U(r_{\text{ps}})}{\partial M} \frac{dM}{dr_h} + \frac{\partial U(r_{\text{ps}})}{\partial P} \frac{dP}{dr_h} + \frac{\partial U(r_{\text{ps}})}{\partial r_{\text{ps}}} \frac{dr_{\text{ps}}}{dr_h}, \quad (3.13)$$

where the last term  $\partial U(r_{\text{ps}})/\partial r_{\text{ps}}$  vanishes identically since  $r_{\text{ps}}$  satisfies the photon-sphere condition

$$\left. \frac{\partial U(r)}{\partial r} \right|_{r=r_{\text{ps}}} = 0. \quad (3.14)$$

The remaining partial derivatives for the RN-AdS spacetime are

$$\frac{\partial U(r_0)}{\partial M} = -\frac{2}{r_0^3}, \quad \frac{\partial U(r_{\text{ps}})}{\partial M} = -\frac{2}{r_{\text{ps}}^3}, \quad (3.15)$$

and

$$\frac{\partial U(r_0)}{\partial P} = \frac{\partial U(r_{\text{ps}})}{\partial P} = \frac{8\pi}{3}. \quad (3.16)$$

Substituting these results into Eq. (3.11) yields

$$hg = k_1 \frac{dM}{dr_h} + k_2 \frac{dP}{dr_h}, \quad (3.17)$$

with

$$k_1 = \frac{2h^2}{r_{\text{ps}}^3} - \frac{2}{r_0^3}, \quad k_2 = \frac{8\pi(1-h^2)}{3}. \quad (3.18)$$

Both coefficients satisfy  $k_1, k_2 \geq 0$ , with equality attained only when  $r_0 = r_{\text{ps}}$ . The nonnegativity of  $k_2$  follows directly from  $0 \leq h \leq 1$ , while  $k_1$  can be rewritten as

$$k_1 = \frac{2}{r_0^2} \left[ \frac{f(r_0)}{f(r_{\text{ps}})} \frac{1}{r_{\text{ps}}} - \frac{1}{r_0} \right], \quad (3.19)$$

which is manifestly nonnegative for  $r_0 \geq r_{\text{ps}}$ . These results demonstrate that the monotonic behavior of  $\xi_c(r_h)$  is jointly controlled by  $dM/dr_h$  and  $dP/dr_h$ .

In the isobaric ensemble the pressure is fixed,  $dP/dr_h = 0$ , and the monotonic behavior of  $\xi_c(r_h)$  is therefore entirely governed by  $dM/dr_h$ . As discussed above, the first law enforces  $dM/dr_h > 0$  on the physical branch, which directly implies that  $\xi_c(r_h)$  is monotonic for all  $r_h > r_{h,\text{min}}$ . Moreover, since  $r_{\text{ps}}(r_h)$  increases monotonically with  $r_h$  (see Fig. 2), it approaches the observer position  $r_0$  as  $r_h$  grows, which has two direct consequences. First, the coefficient  $k_1$  tends to zero, causing  $d\xi_c/dr_h$  to vanish and the shadow evolution to flatten. Second, the observer becomes effectively closer to the black hole in an optical sense, driving the shadow angle toward  $\xi_c \rightarrow 90^\circ$ .

By contrast, in the isothermal ensemble the pressure is no longer fixed but exhibits a characteristic van der Waals-like behavior, so that both  $dM/dr_h$  and  $dP/dr_h$  contribute. Differentiating Eqs. (3.5) and (3.6) with respect to  $r_h$  yields

$$\frac{dM}{dr_h} = \frac{-6Q^2 + r_h^2 + 12\pi T_0 r_h^3}{3r_h^2}, \quad (3.20)$$

$$\frac{dP}{dr_h} = \frac{-2Q^2 + r_h^2 - 2\pi T_0 r_h^3}{4\pi r_h^5}. \quad (3.21)$$

from which it follows immediately that both derivatives are negative as  $r_h \rightarrow 0$ , while for  $r_h \rightarrow \infty$  one has  $dM/dr_h > 0$  and  $dP/dr_h \rightarrow 0$ . Substituting these signs into Eq. (3.17) shows that  $hg < 0$  at small  $r_h$  and  $hg > 0$  at large  $r_h$ , implying that  $\xi_c(r_h)$  is globally nonmonotonic—in sharp contrast to the isobaric case. This nonmonotonic behavior of the shadow size can therefore serve as a clear diagnostic for distinguishing isothermal from isobaric evolution. Moreover, as in the isobaric ensemble, for sufficiently small or sufficiently large  $r_h$  one finds  $r_{ps} \rightarrow r_0$  (see Fig. 2), so that  $d\xi_c/dr_h \rightarrow 0$  and  $\xi_c \rightarrow 90^\circ$ .

To verify the above analysis, we present numerical results for the shadow angle  $\xi_c(r_h)$  at  $Q = 0.5$  and  $Q = 1$ . Figures 3 and 4 correspond to the isobaric ensemble, while Figs. 5 and 6 show the isothermal ensemble, with the blue solid curves representing  $\xi_c(r_h)$  in all cases. In the isobaric ensemble, once the nonphysical branch is truncated at  $r_{h,min}$ ,  $\xi_c(r_h)$  increases strictly monotonically, with a progressively flattening slope and an asymptotic approach to  $\xi_c = 90^\circ$ . By contrast, in the isothermal ensemble  $\xi_c(r_h)$  exhibits a nonmonotonic behavior, decreasing at small  $r_h$  and increasing again at larger  $r_h$ , while becoming flat and approaching  $90^\circ$  in both limits. These numerical results are in precise agreement with Eq. (3.17) and the preceding analytic arguments.

In the same figures we also display the numerical results for the angular sizes  $\xi_n(r_h)$  of accretion-disk images. The red solid curves correspond to the primary images produced by emitters on the  $r = r_{isco}$  orbit, while the orange and green dashed curves represent the secondary images generated by emitters on the  $r = r_{isco}$  and  $r \rightarrow \infty$  orbits, respectively. Note that we do not plot the primary image associated with  $r \rightarrow \infty$ , since it appears excessively large to the observer, with an angular size that never falls below  $90^\circ$ .

These plots reveal a striking feature: the monotonic behavior of  $\xi_n(r_h)$  is identical to that of the shadow angle  $\xi_c(r_h)$ , and their extrema occur at the same values of  $r_h$ . This demonstrates that the nonmonotonic evolution of accretion-disk images can serve as the same diagnostic for distinguishing isobaric and isothermal ensembles as the black hole shadow. From an observational perspective, accretion disks are particularly appealing because they are intrinsically luminous and do not require an idealized background light source, making them a more accessible probe of black hole thermodynamic evolution.

We also note an intriguing phenomenon present in these figures: the angular size of the primary image associated with  $r = r_{isco}$  can be smaller than that of the corresponding secondary image. Similar effects have been discussed in previous studies, and we defer a detailed investigation of this behavior to future work.

Note that the above discussion has not yet taken black hole phase transitions into account, whose presence breaks the otherwise continuous evolution of black hole images and may therefore encode additional thermodynamic information. To this end, the small- and large-black hole radii at the phase

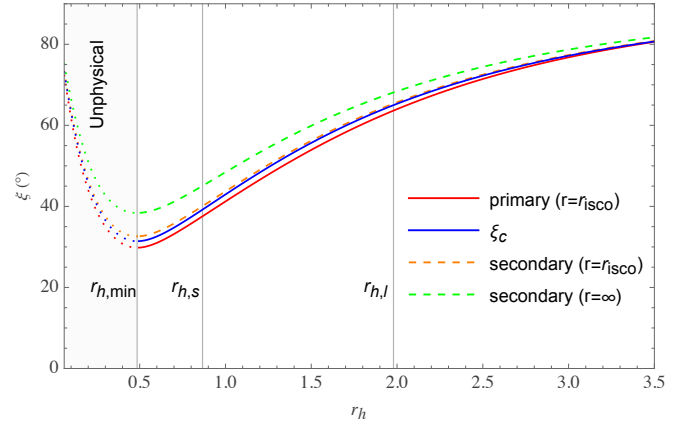


FIG. 3. Evolution of the black hole shadow angle  $\xi_c$  and the accretion-disk image angle  $\xi_n$  as functions of the horizon radius  $r_h$  in the isobaric ensemble, with  $Q = 0.5$  and  $P = 0.8 P_c$ .

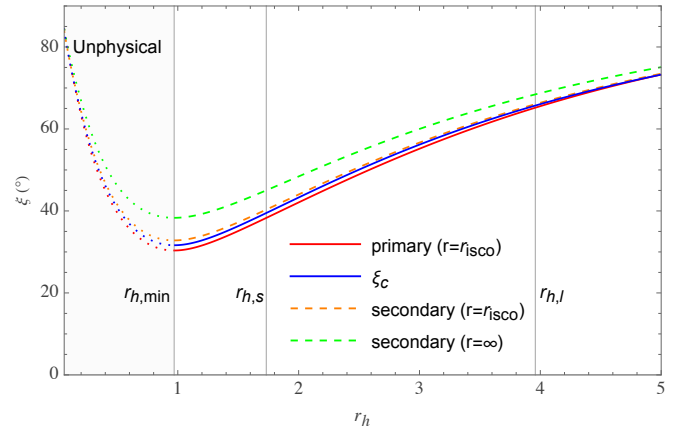


FIG. 4. Evolution of the black hole shadow angle  $\xi_c$  and the accretion-disk image angle  $\xi_n$  as functions of the horizon radius  $r_h$  in the isobaric ensemble, with  $Q = 1$  and  $P = 0.8 P_c$ .

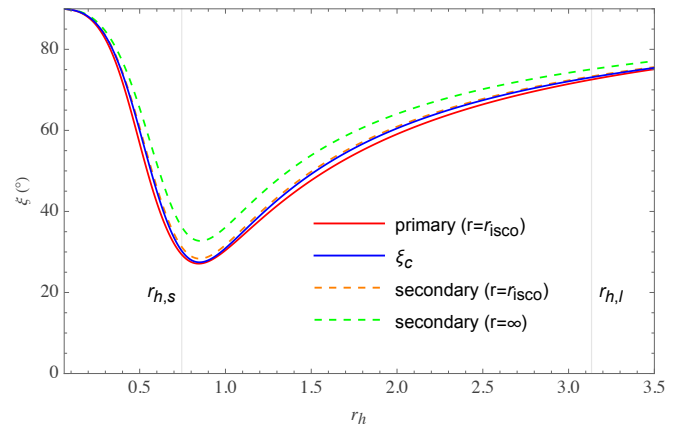


FIG. 5. Evolution of the black hole shadow angle  $\xi_c$  and the accretion-disk image angle  $\xi_n$  as functions of the horizon radius  $r_h$  in the isothermal ensemble, with  $Q = 0.5$  and  $T_0 = 0.8 T_c$ .



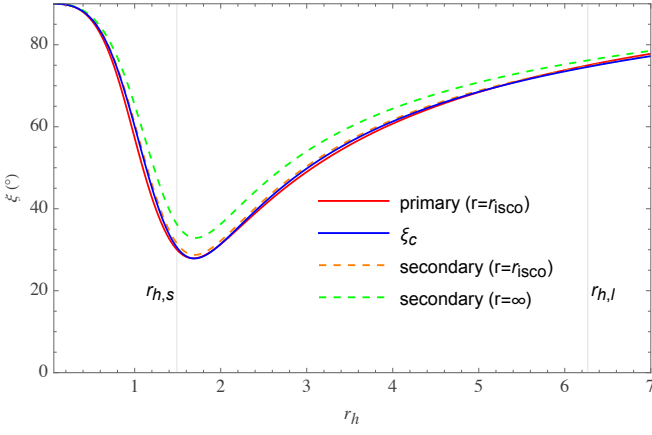


FIG. 6. Evolution of the black hole shadow angle  $\xi_c$  and the accretion-disk image angle  $\xi_n$  as functions of the horizon radius  $r_h$  in the isothermal ensemble, with  $Q = 1$  and  $T_0 = 0.8 T_c$ .

transition,  $r_{h,s}$  and  $r_{h,l}$ , determined via the Maxwell equal-area construction, are marked in Figs. 3–6. At these radii the otherwise continuous evolution of the image size  $\xi(r_h)$  (including both  $\xi_c(r_h)$  and  $\xi_n(r_h)$ ) is interrupted by a discontinuous jump, which immediately raises two natural questions. First, does the black hole image always increase across the transition, namely  $\xi(r_{h,l}) > \xi(r_{h,s})$ ? Second, is the monotonic behavior of  $\xi(r_h)$  the same before and after the transition?

For the isobaric ensemble the answers are straightforward. Since  $\xi(r_h)$  is strictly monotonically increasing in the isobaric ensemble, one necessarily has  $\xi(r_{h,l}) > \xi(r_{h,s})$ , implying a sudden increase of the image size across the phase transition and supporting earlier proposals that black hole phase transitions may be diagnosed through abrupt changes in optical observables. Moreover,  $\xi(r_h)$  remains monotonically increasing on both sides of the transition.

The situation is qualitatively different in the isothermal ensemble, because  $\xi(r_h)$  is nonmonotonic. In this case several distinct possibilities arise depending on the relative ordering of the small-black hole radius  $r_{h,s}$ , the large-black hole radius  $r_{h,l}$ , and the extremum position  $r_{h,e}$  of  $\xi(r_h)$ .

Specifically,

- (i) if  $r_{h,s} < r_{h,l} < r_{h,e}$ , one finds  $\xi(r_{h,l}) < \xi(r_{h,s})$ , with  $\xi(r_h)$  decreasing before the transition and exhibiting a decrease followed by an increase afterward;
- (ii) if  $r_{h,s} \leq r_{h,e} \leq r_{h,l}$ , then  $\xi(r_{h,l})$  may be larger than, smaller than, or equal to  $\xi(r_{h,s})$ , while  $\xi(r_h)$  decreases before the transition and increases afterward;
- (iii) if  $r_{h,e} < r_{h,s} < r_{h,l}$ , one has  $\xi(r_{h,l}) > \xi(r_{h,s})$ , with  $\xi(r_h)$  exhibiting a decrease followed by an increase before the transition and a monotonic increase afterward.

The configurations displayed in Figs. 5 and 6 correspond to case (ii) with  $\xi(r_{h,l}) > \xi(r_{h,s})$ . It is worth noting that all three cases preserve the nonmonotonic evolution of black hole images along isotherms, indicating that the inclusion of a phase transition does not invalidate the criterion based on nonmonotonicity for distinguishing isobaric from isothermal ensembles. To clarify which of these possibilities can actually occur, we proceed in two steps: we first analyze the relative ordering

of  $r_{h,e}$ ,  $r_{h,s}$ , and  $r_{h,l}$ , and then examine the relation between  $\xi(r_{h,l})$  and  $\xi(r_{h,s})$ .

To implement these two steps, the most straightforward strategy is to determine  $r_{h,e}$ ,  $r_{h,s}$ ,  $r_{h,l}$  and the corresponding image sizes  $\xi(r_{h,s})$  and  $\xi(r_{h,l})$  for all admissible black hole parameters. For RN-AdS black holes in the isothermal ensemble, the admissible parameters are the charge  $Q$  and the temperature  $T_0$ . Fortunately, the dependence on the charge  $Q$  can be eliminated by introducing reduced (dimensionless) variables,

$$\tilde{r}_h = \frac{r_h}{r_{h,c}}, \quad \tilde{M} = \frac{M}{M_c}, \quad \tilde{P} = \frac{P}{P_c}, \quad \tilde{T} = \frac{T}{T_c}, \quad (3.22)$$

where

$$r_{h,c} = \sqrt{6} Q, \quad M_c = \frac{2\sqrt{6} Q}{3}, \quad (3.23)$$

$$P_c = \frac{1}{96\pi Q^2}, \quad T_c = \frac{1}{3\sqrt{6}\pi Q},$$

are the critical values at the thermodynamic critical point. In particular,  $r_{h,c}$  and  $T_c$  are determined by the criticality conditions

$$\left(\frac{\partial P}{\partial r_h}\right)_T = 0, \quad \left(\frac{\partial^2 P}{\partial r_h^2}\right)_T = 0, \quad (3.24)$$

and substituting these into Eqs. (3.5) and (3.6) yields the corresponding critical mass  $M_c$  and pressure  $P_c$ . In addition, since the observer position  $r_0$  is freely chosen and does not possess an intrinsic critical value, we rescale it by the critical horizon radius,

$$\tilde{r}_0 = \frac{r_0}{r_{h,c}}. \quad (3.25)$$

Substituting these reduced variables into Eqs. (3.5) and (3.6) yields

$$\tilde{M}(\tilde{r}_h) = \frac{2 + 6\tilde{r}_h^2 + 12\sqrt{6}\pi\tilde{T}_0\tilde{r}_h^3}{18\tilde{r}_h}, \quad (3.26)$$

$$\tilde{P}(\tilde{r}_h) = \frac{12 - \tilde{r}_h^2 + 24\pi\tilde{T}_0\tilde{r}_h^3}{96\tilde{r}_h^4}, \quad (3.27)$$

which are manifestly independent of the charge  $Q$ , implying that all results obtained from them are universal and valid for arbitrary  $Q$ . Likewise, the shadow angle  $\xi_c$  can be expressed in terms of the reduced variables and thus no longer depends explicitly on the charge  $Q$ ,

$$\xi_c = \xi_c(\tilde{r}_h; \tilde{r}_0, \tilde{T}_0). \quad (3.28)$$

After this reduction, only a single control parameter, the reduced temperature  $\tilde{T}_0$  (equivalently  $T_0$ ), remains, allowing all relevant cases to be systematically explored through a numerical scan over  $\tilde{T}_0$ . It should be noted that the requirement  $\tilde{P}(\tilde{r}_h) \geq 0$  for all admissible  $\tilde{r}_h$  imposes a lower bound on the temperature,  $\tilde{T}_0 \geq \sqrt{2}/2$ , so that the physically relevant range is  $\tilde{T}_0 \in [\sqrt{2}/2, 1]$ .

We now address the first step outlined above. Applying the Maxwell equal-area construction to Eq. (3.27) yields the reduced small- and large-black hole radii  $\tilde{r}_{h,s}(\tilde{T}_0)$  and  $\tilde{r}_{h,l}(\tilde{T}_0)$ , while solving  $\partial\xi_c/\partial\tilde{r}_h = 0$  from Eq. (3.28) determines the extremal radius  $\tilde{r}_{h,e}(\tilde{T}_0, \tilde{T}_0)$ . These quantities are displayed in Figure 7, where the black solid and dashed curves denote  $\tilde{r}_{h,s}(\tilde{T}_0)$  and  $\tilde{r}_{h,l}(\tilde{T}_0)$ , respectively, meeting at point A(1, 1) that corresponds to  $r_{h,s} = r_{h,l} = r_{h,c}$ . The four colored solid curves show  $\tilde{r}_{h,e}(\tilde{T}_0, \tilde{T}_0)$  for different values of  $\tilde{T}_0$ .

It is evident from Fig. 7 that throughout the allowed range of  $\tilde{T}_0$  one always has  $\tilde{r}_{h,l} > \tilde{r}_{h,e}$ , so that the previously discussed case (i) never occurs. Cases (ii) and (iii) are separated by the intersection of  $\tilde{r}_{h,s}$  and  $\tilde{r}_{h,e}$  shown in the figure. We define the temperature at this intersection as the critical reduced temperature  $\tilde{T}_{0,c}$ , which gives rise to the following two regimes:

- (a) For  $\tilde{T}_0 \leq \tilde{T}_{0,c}$  one has  $\tilde{r}_{h,s} \leq \tilde{r}_{h,e} < \tilde{r}_{h,l}$ , corresponding to case (ii), in which the shadow angle  $\xi_c(r_h)$  decreases monotonically before the phase transition and increases monotonically afterward;
- (b) For  $\tilde{T}_0 > \tilde{T}_{0,c}$  one finds  $\tilde{r}_{h,e} < \tilde{r}_{h,s} < \tilde{r}_{h,l}$ , corresponding to case (iii), where  $\xi_c(r_h)$  first decreases and then increases before the transition and increases monotonically afterward.

These results demonstrate that black hole phase transition not only induces a discontinuous jump in the image size, but, under isothermal evolution, also allows one to distinguish two distinct temperature regimes,  $\tilde{T}_0 \leq \tilde{T}_{0,c}$  and  $\tilde{T}_0 > \tilde{T}_{0,c}$ , from the black hole shadow size, revealing additional thermodynamic information encoded in black hole images. The same conclusion is expected to hold for accretion-disk images, since their angular sizes  $\xi_n(r_h)$  exhibit the same qualitative behavior as  $\xi_c(r_h)$ . To confirm this expectation, we numerically plot  $\xi(r_h)$  for  $\tilde{T}_0 = \tilde{T}_{0,c}$  (Fig. 8) and for  $\tilde{T}_0 > \tilde{T}_{0,c}$  (Fig. 9), finding full agreement with the above analysis.

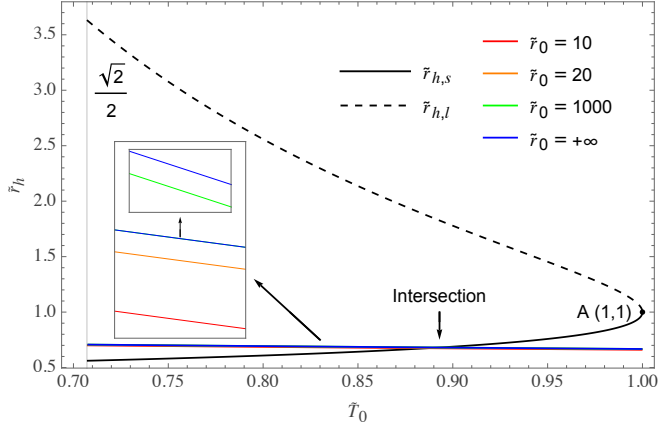


FIG. 7. Reduced small-, large-, and extremal-radius curves,  $\tilde{r}_{h,s}$ ,  $\tilde{r}_{h,l}$ , and  $\tilde{r}_{h,e}$ , as functions of the reduced temperature  $\tilde{T}_0$ .

We now turn to the second step outlined above. This is straightforward: inserting the previously obtained reduced radii  $\tilde{r}_{h,s}(\tilde{T}_0)$  and  $\tilde{r}_{h,l}(\tilde{T}_0)$  into Eq. (3.28) directly yields the corresponding shadow angles. The results are displayed in Fig. 10, where the colored solid and dashed curves represent

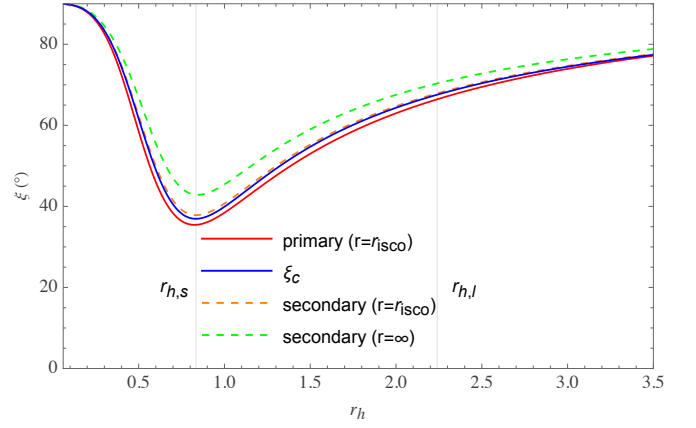


FIG. 8. Evolution of the black hole shadow angle  $\xi_c$  and the accretion-disk image angle  $\xi_n$  as functions of the horizon radius  $r_h$  in the isothermal ensemble, with  $Q = 0.5$  and  $\tilde{T}_0 = \tilde{T}_{0,c}$ .

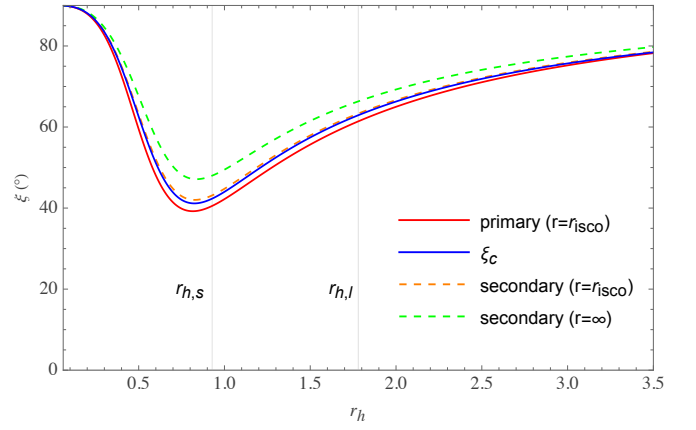


FIG. 9. Evolution of the black hole shadow angle  $\xi_c$  and the accretion-disk image angle  $\xi_n$  as functions of the horizon radius  $r_h$  in the isothermal ensemble, with  $Q = 0.5$  and  $\tilde{T}_0 > \tilde{T}_{0,c}$ .

$\xi_c(\tilde{r}_{h,s})$  and  $\xi_c(\tilde{r}_{h,l})$ , respectively. One clearly finds that, for both  $\tilde{T}_0 \leq \tilde{T}_{0,c}$  [case (ii)] and  $\tilde{T}_0 > \tilde{T}_{0,c}$  [case (iii)],

$$\xi_c(\tilde{r}_{h,l}) \geq \xi_c(\tilde{r}_{h,s}), \quad (3.29)$$

with equality attained only at  $\tilde{T}_0 = 1$ , where  $\tilde{r}_{h,s} = \tilde{r}_{h,l} = \tilde{r}_{h,c}$ . Therefore, although  $\xi_c(r_h)$  is nonmonotonic along isothermal evolution, the black hole shadow nevertheless always increases across the phase transition, mirroring the isobaric case. This implies that a sudden enlargement of the shadow alone can signal the occurrence of a phase transition, but is insufficient to distinguish between isobaric and isothermal evolution.

The same conclusion is expected to hold for accretion-disk images. On the one hand, Figs. 5 and 6 show that  $\xi_n(r_h)$  closely tracks  $\xi_c(r_h)$ , with the difference between the two remaining small (typically below  $10^\circ$ ). On the other hand, Fig. 10 indicates that for  $\tilde{T}_0 \leq \tilde{T}_{0,c} \simeq 0.89$  (see Fig. 7), the shadow-angle gap between  $\xi_c(\tilde{r}_{h,s})$  and  $\xi_c(\tilde{r}_{h,l})$  is large (at least  $30^\circ$ ), so that  $\xi_n(\tilde{r}_{h,s})$  can never approach  $\xi_n(\tilde{r}_{h,l})$ .

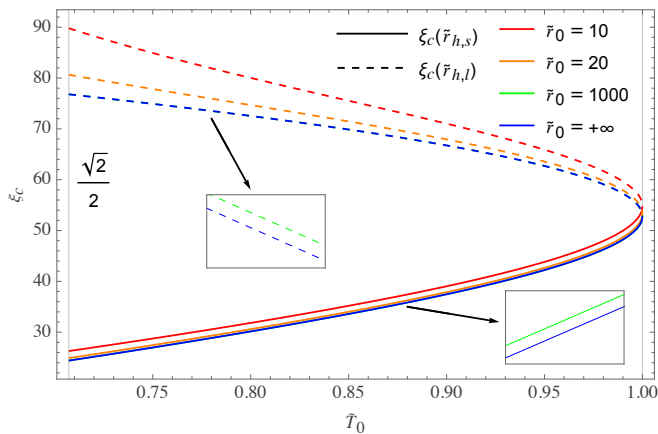


FIG. 10. Shadow angle  $\xi_c$  evaluated at the reduced small- and large-black-hole radii  $\tilde{r}_{h,s}$  and  $\tilde{r}_{h,l}$  as a function of the reduced temperature  $\tilde{T}_0$ .

#### IV. CONCLUSIONS

In this work we have investigated how the images of RN–AdS black holes evolve along isobaric and isothermal thermodynamic processes. Our results show that black hole images encode not only information about phase transitions, but also about the underlying thermodynamic ensemble, and, in the isothermal case, even about the temperature.

Phase transition information encoded in black hole images has long been recognized, particularly in the isobaric ensemble, where numerous studies have shown that a thermodynamic phase transition manifests itself as a sudden change in the image size. In this paper, we extend this conclusion to the isothermal ensemble and demonstrate that, in both ensembles, the phase transition always leads to a sudden increase of the black hole image, rather than a decrease or no change. While this result further confirms the robustness of using image discontinuities to detect black hole phase transitions, it also implies that such abrupt changes alone are generally insufficient to distinguish whether the underlying thermodynamic evolution is isobaric or isothermal.

Fortunately, we find that black hole images exhibit qualitatively different evolution patterns in the two ensembles. Along isobars, the image size grows monotonically with the horizon radius  $r_h$ , whereas along isotherms it first decreases and then increases. This contrast implies that the nonmonotonic be-

havior of the image size itself provides a diagnostic for distinguishing isobaric from isothermal processes.

Going further, we find that when the black hole evolves along an isothermal path, the nonmonotonic behavior of the image size introduces an extremal radius. Depending on its ordering relative to the small- and large-black hole radii at the phase transition, three distinct evolutionary patterns are possible in principle. We demonstrate, however, that only two of them are physically realized, and that they are separated by a critical reduced temperature  $\tilde{T}_{0,c}$ . For  $\tilde{T}_0 \leq \tilde{T}_{0,c}$ , the image size decreases monotonically with  $r_h$  before the transition and increases monotonically afterward. By contrast, for  $\tilde{T}_0 > \tilde{T}_{0,c}$ , the image size first decreases and then increases as a function of  $r_h$  before the transition, while still increasing monotonically afterward. These two clearly distinct behaviors provide a direct observational criterion for discriminating between different temperature ranges in the isothermal ensemble.

It is worth emphasizing that we establish a new paradigm for extracting black hole information by jointly considering phase transitions and the nonmonotonic evolution of black hole images. Compared with approaches that focus solely on phase transitions or on image monotonicity, this combined perspective allows additional thermodynamic information—most notably the temperature—to be inferred from imaging observables. We expect that this paradigm can be extended to other black hole systems, including higher-curvature or nonlinear-electrodynamics black holes exhibiting rich phase structures. Applying the same framework to such systems may reveal additional thermodynamic information encoded in their optical appearances.

Finally, we emphasize that we do not claim astrophysical black holes to follow idealized isobaric or isothermal trajectories in a strict sense. Real black hole evolution is governed by a variety of processes—such as accretion, environmental interactions, and Hawking radiation—and is unlikely to be captured by a single thermodynamic path. Our results are instead intended to clarify, at a conceptual level, how thermodynamic information can leave imprints on optical observables, thereby broadening the range of tools available for probing the microscopic physics of black holes.

#### ACKNOWLEDGMENTS

This work is supported in part by NSFC Grants No. 12165005 and No. 11961131013.

- [1] K. Akiyama *et al.* (Event Horizon Telescope Collaboration), First M87 Event Horizon Telescope results. VI. The shadow and mass of the central black hole, *Astrophys. J. Lett.* **875**, L6 (2019).
- [2] P. V. P. Cunha, N. A. Eiró, C. A. R. Herdeiro, and J. P. S. Lemos, Lensing and shadow of a black hole surrounded by a heavy accretion disk, *J. Cosmol. Astropart. Phys.* **03** (2020) 035.
- [3] A. Naveena Kumara, C. L. Ahmed Rizwan, S. Punacha, K. M. Ajith, and M. S. Ali, Photon orbits and thermodynamic

phase transition of regular AdS black holes, *Phys. Rev. D* **102**, 084059 (2020).

- [4] Y.-M. Xu, H.-M. Wang, Y.-X. Liu, and S.-W. Wei, Photon sphere and reentrant phase transition of charged Born-Infeld-AdS black holes, *Phys. Rev. D* **100**, 104044 (2019).
- [5] M. Chabab, H. El Moumni, S. Iraoui, and K. Masmar, Probing correlation between photon orbits and phase structure of charged AdS black hole in massive gravity background, *Int. J. Mod. Phys. A* **34**, 1950231 (2020).



- [6] M. Guerrero, G.J. Olmo, D. Rubiera-Garcia, and D.S.-C. Gómez, Shadows and optical appearance of black bounces illuminated by a thin accretion disk, *J. Cosmol. Astropart. Phys.* **08** (2021) 036.
- [7] T. Bronzwaer and H. Falcke, The nature of black hole shadows, *Astrophys. J.* **920**, 155 (2021).
- [8] Y.-Z. Du, H.-F. Li, F. Liu, and L.-C. Zhang, Photon orbits and phase transition for non-linear charged anti-de Sitter black holes, *J. High Energy Phys.* **01** (2023) 137.
- [9] J. Yang, C. Zhang, and Y. Ma, Shadow and stability of quantum-corrected black holes, *Eur. Phys. J. C* **83**, 619 (2023).
- [10] L. You, Y.-H. Feng, R.-B. Wang, X.-R. Hu, and J.-B. Deng, Decoding quantum gravity information with black hole accretion disk, *Universe* **10**, 393 (2024).
- [11] L. You, R.-b. Wang, S.-J. Ma, J.-B. Deng, and X.-R. Hu, Optical properties of Euler-Heisenberg black hole in the Cold Dark Matter Halo, [arXiv:2403.12840](https://arxiv.org/abs/2403.12840).
- [12] S. W. Hawking and D. N. Page, Thermodynamics of black holes in anti-de Sitter space, *Commun. Math. Phys.* **87**, 577 (1983).
- [13] D. Kastor, S. Ray, and J. Traschen, Enthalpy and the mechanics of AdS black holes, *Classical Quantum Gravity* **26**, 195011 (2009).
- [14] B.P. Dolan, The cosmological constant and black-hole thermodynamic potentials, *Classical Quantum Gravity* **28**, 125020 (2011).
- [15] M. Cvetic, G. W. Gibbons, D. Kubiznak, and C. N. Pope, Black hole enthalpy and an entropy inequality for the thermodynamic volume, *Phys. Rev. D* **84**, 024037 (2011).
- [16] R. Banerjee and D. Roychowdhury, Thermodynamics of phase transition in higher dimensional AdS black holes, *J. High Energy Phys.* **11** (2011) 004.
- [17] R. Banerjee, S. K. Modak, and D. Roychowdhury, A unified picture of phase transition: From liquid-vapour systems to AdS black holes, *J. High Energy Phys.* **10** (2012) 125.
- [18] D. Kubiznak and R. B. Mann, P-V criticality of charged AdS black holes, *J. High Energy Phys.* **07** (2012) 033.
- [19] S.-W. Wei and Y.-X. Liu, Critical phenomena and thermodynamic geometry of charged Gauss-Bonnet AdS black holes, *Phys. Rev. D* **87**, 044014 (2013).
- [20] R.-G. Cai, L.-M. Cao, L. Li, and R.-Q. Yang, P-V criticality in the extended phase space of Gauss-Bonnet black holes in AdS space, *J. High Energy Phys.* **09** (2013) 005.
- [21] N. Altamirano, D. Kubizňák, R. B. Mann, and Z. Sherkatghanad, Kerr-AdS analogue of triple point and solid/liquid/gas phase transition, *Classical Quantum Gravity* **31**, 042001 (2014).
- [22] N. Altamirano, D. Kubiznak, and R. B. Mann, Reentrant phase transitions in rotating anti-de Sitter black holes, *Phys. Rev. D* **88**, 101502 (2013).
- [23] A. M. Frassino, D. Kubiznak, R. B. Mann, and F. Simovic, Multiple reentrant phase transitions and triple points in Lovelock thermodynamics, *J. High Energy Phys.* **09** (2014) 080.
- [24] S.-W. Wei and Y.-X. Liu, Triple points and phase diagrams in the extended phase space of charged Gauss-Bonnet black holes in AdS space, *Phys. Rev. D* **90**, 044057 (2014).
- [25] D. Kubiznak, R. B. Mann, and M. Teo, Black hole chemistry: Thermodynamics with Lambda, *Classical Quantum Gravity* **34**, 063001 (2017).
- [26] S.-W. Wei and Y.-X. Liu, Photon orbits and thermodynamic phase transition of  $d$ -dimensional charged AdS black holes, *Phys. Rev. D* **97**, 104027 (2018).
- [27] S.-W. Wei, Y.-X. Liu, and Y.-Q. Wang, Probing the relationship between the null geodesics and thermodynamic phase transition for rotating Kerr-AdS black holes, *Phys. Rev. D* **99**, 044013 (2019).
- [28] M. Zhang, S.-Z. Han, J. Jiang, and W.-B. Liu, Circular orbit of a test particle and phase transition of a black hole, *Phys. Rev. D* **99**, 065016 (2019).
- [29] M. Zhang and M. Guo, Can shadows reflect phase structures of black holes?, *Eur. Phys. J. C* **80**, 790 (2020).
- [30] L. You and J. Yang, Revisiting particle circular orbits as probes of black hole thermodynamics, [arXiv:2512.17642](https://arxiv.org/abs/2512.17642).
- [31] V. Perlick and O. Y. Tsupko, Calculating black hole shadows: Review of analytical studies, *Phys. Rept.* **947**, 1 (2022).